metals

Article

Quasi-Static, Dynamic Compressive Properties and Deformation Mechanisms of Ti-6Al-4V Alloy with Gradient Structure

Lei Lei [1,2,*], Yongqing Zhao [1,2,*], Qinyang Zhao [3], Shewei Xin [2], Cong Wu [2], Weiju Jia [2] and Weidong Zeng [1]

1 State Key Laboratory of Solidification Processing, Northwestern Polytechnical University, Xi'an 710072, China; zengwd@nwpu.edu.cn
2 Northwest Institute for Nonferrous Metal Research, Xi'an 710016, China; nwpu_xsw@126.com (S.X.); cong_wu@163.com (C.W.); diana_1025@126.com (W.J.)
3 School of Material Science and Engineering, Chang'an University, Xi'an 710064, China; zqy@chd.edu.cn
* Correspondence: leileiacute@126.com (L.L.); trc@c-nin.com (Y.Z.)

Abstract: Gradient structure metals have good comprehensive properties of strength and toughness and are expected to improve the dynamic mechanical properties of materials. However, there are few studies on the dynamic mechanical properties of gradient structured materials, especially titanium alloys. Therefore, in this study, ultrasonic surface rolling is used to prepare a gradient structure layer on the surface of Ti-6Al-4V, and the quasi-static and dynamic compressive properties of coarse-grained Ti-6Al-4V (CG Ti64) and gradient-structured Ti-6Al-4V (GS Ti64) are investigated. The results show that a GS with a thickness of 293 μm is formed. The quasi-static compressive strength of GS Ti64 is higher than that of CG Ti64. Both CG Ti64 and GS Ti64 exhibit weak strain hardening effects and strain rate insensitivity during dynamic compression, and the compressive strength is not significantly improved. The lateral expansion of CG Ti64 is more obvious, while the lateral side of GS Ti64 is relatively straight, indicating that uniform deformation occurs in GS Ti64. The α phase in the GS produces dislocation cells and local deformation bands, and the lamellar structure is transformed into ultrafine crystals after dynamic compression. Both of them produce an adiabatic shear band under 2700 s^{-1}, a large crack forms in CG Ti64, while GS Ti64 forms a small crack, indicating that GS Ti64 has better resistance to damage. The synergistic deformation of GS and CG promotes Ti-6Al-4V to obtain good dynamic mechanical properties.

Keywords: Ti-6Al-4V alloy; ultrasonic surface rolling process; gradient structure; dynamic compression

Citation: Lei, L.; Zhao, Y.; Zhao, Q.; Xin, S.; Wu, C.; Jia, W.; Zeng, W. Quasi-Static, Dynamic Compressive Properties and Deformation Mechanisms of Ti-6Al-4V Alloy with Gradient Structure. *Metals* **2021**, *11*, 1928. https://doi.org/10.3390/met11121928

Academic Editor: Tilmann Beck

Received: 20 October 2021
Accepted: 26 November 2021
Published: 29 November 2021

1. Introduction

Ti-6Al-4V alloy is widely used in aviation, aerospace and marine industries due to its excellent comprehensive mechanical properties [1–4]. During the process of service, it will inevitably be subjected to impact loads, such as planes hit by birds, aircraft landing gears subjected to ground impact, and ships hitting rocks. Therefore, in addition to good quasi-static properties, it is also necessary to have good dynamic bearing capacity to ensure its integrity and reliability under dynamic load [5,6].

There are many studies on the dynamic mechanical properties of Ti-6Al-4V [7–15]. Hu et al. [11] studied the effect of strain rate on the mechanical properties of Ti-6Al-4V, and the results showed that the work hardening rate and flow stress increased with the increase of strain rate, and the formation of ASB (adiabatic shear band) resulted in the failure of the material. Lee et al. [12] indicated that the maximum shear stress and failure shear strain of the bimodal structure is higher than that of the equiaxed structure, and ASB is more inclined to form in the equiaxed structure. The results of Zheng et al. [13] showed that ASB is less likely formed in the bimodal structure with the thicker α lamellar in the β matrix.

The above research mainly optimizes the dynamic mechanical properties of Ti-6Al-4V through heat treatment, but the improvement range is limited. Recent studies have shown that both high strength and high plasticity can be achieved by designing gradient nanostructures [16]. Fang et al. [17] processed coarse-grained copper bars by surface mechanical grinding treatment and obtained a gradient nanostructured copper rod. The yield strength of the gradient nanostructured copper rod is increased to twice that of the ordinary copper rod without loss of plasticity. Wu et al. [18] obtained gradient structure IF steel by surface mechanical grinding. During the tensile deformation process, there is a significant strain gradient from the surface to the core, which transforms the uniaxial stress state into a multiaxial stress state, promoting the continuous accumulation and delivery of dislocations, which in turn produces additional work hardening capacity. Recently, Pan et al. [19] introduced a gradient dislocation cell structure into $Al_{0.1}CoCrFeNi$ high entropy alloy using a small-angle reciprocal torsional gradient plastic deformation technique, while keeping the morphology, size and orientation of the original grain unchanged. The strength of graded dislocation cell alloys is 2–3 times that of coarse-grained and fine-grained materials while maintaining good plasticity and stable work hardening.

In conclusion, gradient nanostructured metals have good comprehensive properties of strength and toughness and are expected to improve the dynamic mechanical properties of materials. However, there are relatively few studies on the dynamic mechanical properties of gradient nanostructured materials. Yuan et al. [20] studied the dynamic mechanical properties of gradient nanostructured pure iron and showed that gradient-grained iron has obvious work hardening behavior, and the dynamic strain rate sensitivity of gradient-grained iron is slightly greater than that of coarse-grained iron. Xing et al. [21] indicated that the dynamic shear deformation behavior of 301 stainless steel with gradient structure showed that the dynamic yield strength is 2–3 times that of coarse-grained austenite structure, and the dynamic shear toughness is more than half that of coarse-grained austenite structure. Bian et al. [22] studied the dynamic shear deformation behavior of gradient nanostructured TWIP steel. The gradient structure layer delayed the formation of the shear band on the nanocrystalline surface.

In summary, the gradient structure materials show excellent dynamic mechanical properties, so the gradient structure is expected to further improve the dynamic mechanical properties of the Ti-6Al-4V alloy. However, knowledge on the effect of gradient structures on the dynamic mechanical properties of Ti-6Al-4V alloys is still lacking. Based on this, the strain hardening behavior and strain rate sensitivity of coarse-grained Ti-6Al-4V (CG Ti64) and gradient-structured Ti-6Al-4V (GS Ti64) are systematically studied over a wide range of strain rates under compression, and the corresponding plastic deformation mechanisms and failure behaviors are also investigated.

2. Materials and Methods

The Ti-6Al-4V alloy used in this work was a hot-forged billet supplied by the Northwest Institute for Nonferrous Metals Research, China. The original microstructure was a bimodal structure consisting of 35% equiaxed primary α phase (α_p) and 65% β transformation microstructure (β_t). The β transus temperature was 970 °C ± 5 °C. Specimens with the dimensions of 14 mm × 14 mm × 70 mm were cut from the billet by an electrical spark linear incising machine. The samples were subjected to $\alpha + \beta$ phase field at 900 °C for 1 h, followed by air-cooling to room temperature and then processed into a cylindrical tensile sample with a diameter of 4 mm and a gauge length of 20 mm. An ultrasonic surface rolling process (USRP) is used to process the gauge section of tensile samples to obtain gradient-structured Ti-6Al-4V. The USRP equipment and the rolling process refer to reference [23]. The parameters of USRP were as follows: static force was 900 N, rotation speed was 180 r/min, axial feeding rate was 0.1 mm/min, vibration amplitude was 7 µm, and repeated roll times was 25. Then, two sizes of cylindrical specimens (Φ4 mm × 6 mm was for the quasi-static compression samples, and Φ4 mm × 4 mm was for the dynamic compression samples) were cut from the tensile samples.

The compressive properties of the materials were tested by an Instron 5985 machine at room temperature. Before the test, the upper and lower surfaces of the specimen were smeared with lubricating oil to minimize test errors caused by surface friction. The compression strain rate was 1×10^{-3} s^{-1}. The compression test was repeated three times to confirm the validity of the results. The work hardening rate (Θ) was calculated according to the equation of $\Theta = d\sigma_T/d\varepsilon_T$. The true strain ($\varepsilon_T$) was calculated according to the equation, $\varepsilon_T = \ln(1 + \varepsilon)$, in which ε represents the engineering strain. The true stress (σ_T) was calculated according to the equation, $\sigma_T = \sigma\ (1 + \varepsilon)$, in which σ represents the engineering stress.

The split-Hopkinson pressure bar was used to test the dynamic mechanical properties of the specimens under different high strain rates. At least three samples were tested for each condition to certify reproducibility. To measure the in-depth hardness, cross-sections of the samples were polished. The hardness of the gradient structure layer was tested by an HVS-1000 microhardness tester with a load of 50 gf (0.49 N) and a holding time of 10 s. Three measurements were taken and the average was calculated as the result.

The gradient structure and microstructure after compression deformation were observed by optical microscope (OM, Zeiss Axio vert A1, Germany) scanning electron microscope (SEM, JSM-6700F, JEOL, Tokyo, Japan), field emission SEM (GeminiSEM 500, Zeiss, Oberkochen, Germany) equipped with an electron backscatter diffraction detector (EBSD, Oxford Symmetry, Oxford, UK), and a transmission electron microscopy (TEM, FEI Tecnai G2 F30, Hillsboro, OR, USA). The samples for the EBSD test were grounded with abrasive papers first and then electropolished in a solution consisting of 94 vol.% glacial acetic acid and 6 vol.% perchloric acid ($HClO_4$) at ~60 V for 15 s. The obtained EBSD data was analyzed by AZtecCrystal 2.0 software (Oxford Instrument, Oxford, UK). The TEM sample cutting location and preparation process refer to reference [23]. The schematic diagram of the TEM preparation process is shown in Figure 1. TEM samples were mechanical grinding down to about 50 μm, and then electropolished in a solution consisting of 60 vol.% methanol, 35 vol.% butyl alcohol and 5 vol.% perchloric acid at 30 V and −30 °C by twin-jet electrochemical polisher. TEM experiments were carried out at a voltage of 200 kV.

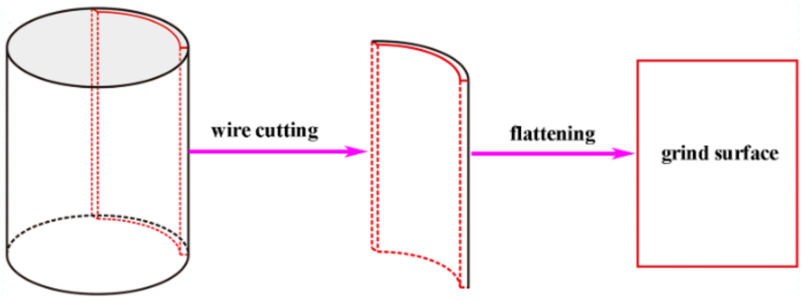

Figure 1. TEM sample preparation process reprinted with permission from Reference [23]. Copyright 2022 Elsevier.

3. Results and Discussion

Gradient Structure Characterization

Figure 2 shows the microstructure of the surface layer of GS Ti64. A circle of obvious plastic deformation layer is formed on the surface, and the microstructure presents an obvious gradient distribution. The microstructure near the surface is severely refined and the primary α phase elongates along the rolling direction. The obvious deformation layer depth of the Ti-6Al-4V alloy induced by USRP is 126 μm ± 12 μm.

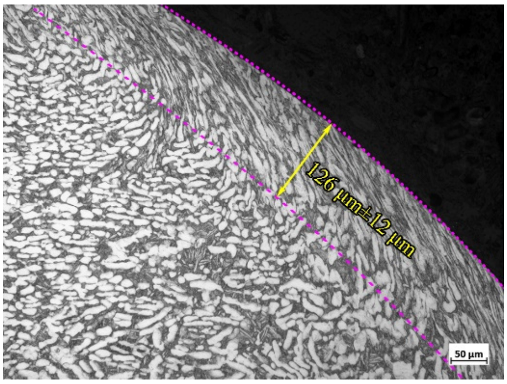

Figure 2. Cross-section microstructure of GS Ti64.

In order to further analyze the gradient structure, EBSD is used to characterize the GS Ti64, as shown in Figure 3. It can be seen from the IPF map (Figure 3) that the region close to the surface shows a black zero resolution area due to severe plastic deformation. Although only the grains near the surface are significantly refined, the color of the grains farther away from the surface is changed, indicating that the USRP causes crystal rotation of the grains farther away from the surface. KAM (kernel average misorientation) value decreased gradually with the increase of the distance from the surface, presenting a gradient distribution (Figure 3b). The KAM value near the surface is high and the distribution is relatively uniform, while the KAM value far away from the surface is unevenly distributed. Local plastic deformation occurred inside the α phase, and the KAM value near the interface is higher. The depth of the plastic affected zone caused by USRP is 293 μm ± 16 μm.

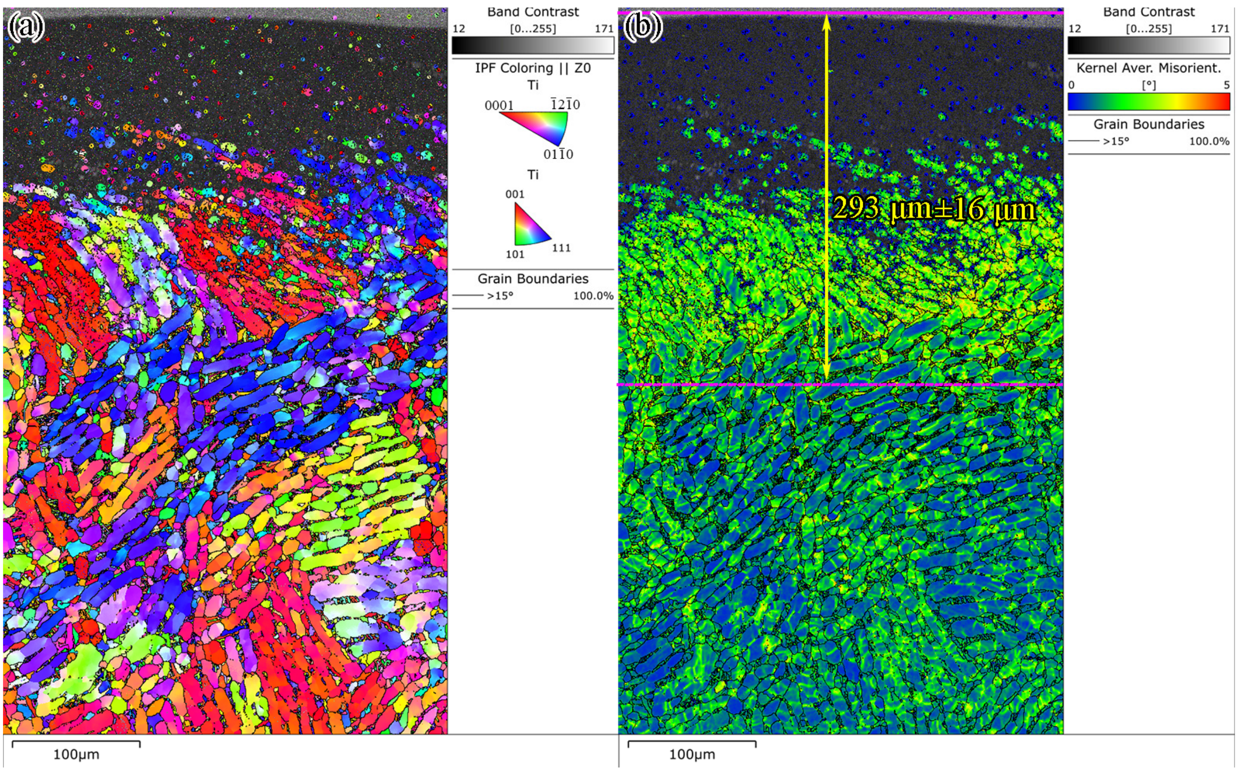

Figure 3. EBSD images of the cross-section of GS Ti64: (**a**) IPF; (**b**) KAM.

TEM is used to observe the microstructure of GS Ti64 at a distance of about 20 μm from the top surface. Figure 4a shows the formation of some lamellar structures, and the

SAED (selected area electron diffraction) pattern derived from the circle region in Figure 4a shows that the lamella has an HCP structure (as shown in the inset of Figure 4a). The HRTEM micrograph shows a clear interface between the lamellae and the matrix. However, the IFFT (inverse fast Fourier transition) result of the yellow square area in Figure 4b shows that the crystal structure of the lamellae is the same as the matrix. The crystal lattice at the interface is complete, but a certain degree of lattice distortion has occurred, indicating that the different degrees of deformation in different regions result in the formation of lamella with low angle grain boundaries (Figure 4c). Figure 4d shows that the large block structure of α phase forms substructures such as dislocation cells and deformed bands. Fine grains are formed in the β_t, the diffraction spots are a series of diffraction rings, indicating the formation of randomly oriented ultrafine/nanocrystal crystals. The enlarged view of the β_t region shows that it is composed of an ultrafine lamellar structure (Figure 4e) and an ultrafine equiaxed crystal structure (Figure 4f).

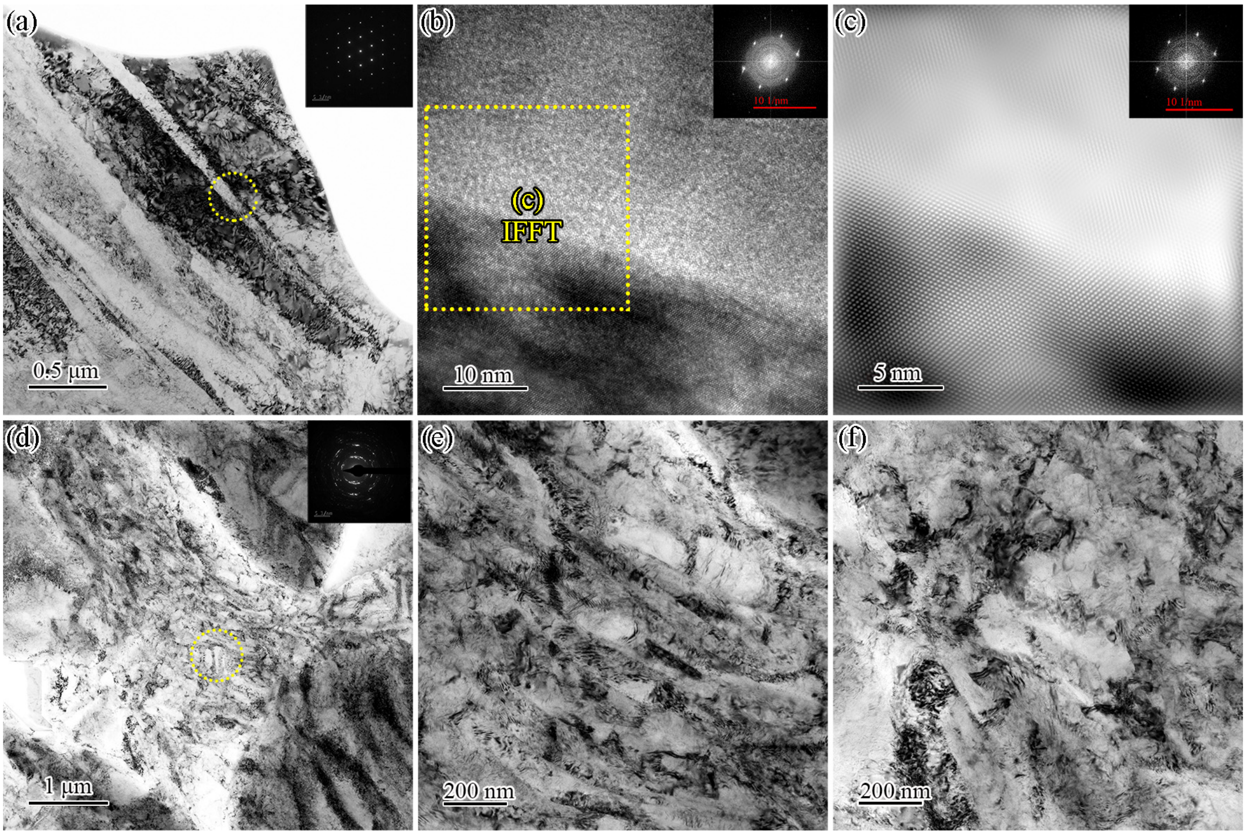

Figure 4. TEM images at 20 µm from the GS Ti64 surface: (**a**) lamellar structure; (**b**) high-resolution image at lamellar interface; (**c**) the IFFT image of the box area in Figure 4b; (**d**) β_t region; (**e**,**f**) the magnification of the β_t region.

The microhardness of the cross-section of the GS Ti64 sample changes with the depth, as shown in Figure 5. The microhardness gradually decreases from the surface to the core. The thickness of the entire gradient deformation layer reaches 325 µm, and the hardness of the topmost layer is about 26% higher than that of the CG matrix. USRP causes severe plastic deformation and grain refinement on the surface of Ti-6Al-4V, resulting in increased hardness. With the increase of the distance from the surface, the degree of plastic deformation and grain refinement gradually weakened, resulting in a gradual decrease in hardness.

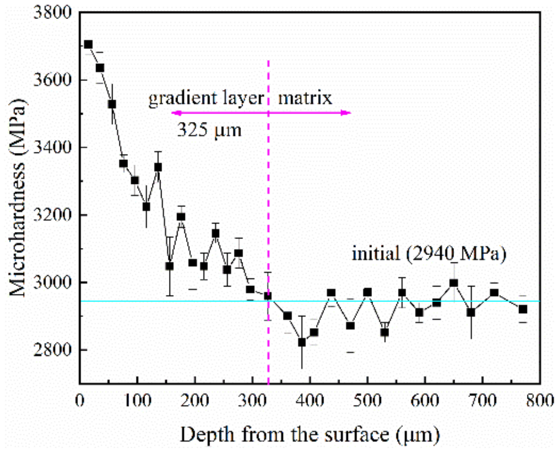

Figure 5. The cross-section hardness gradient distribution of GS Ti64.

Figure 6 shows the engineering and true stress-strain curves of CG Ti64 and GS Ti64. During the compression process, the experiment is stopped when the sample is damaged. The engineering stress of both firstly increases and then decreases with the increase of strain. The fracture strain of GS Ti64 is about 6% higher than that of CG Ti64 (Figure 6a), suggesting that GS Ti64 has better compressive plasticity. The compressive strength of GS Ti64 (1590 MPa $\pm$ 22 MPa) is higher than that of CG Ti64 (1520 MPa $\pm$ 15 MPa), indicating that the gradient structure improves the compression resistance of Ti-6Al-4V. Figure 6b exhibits that the true stress of both increases rapidly with the increase of strain at the initial stage of deformation, and then increases slowly to the peak stress and then decreases gradually until fracture. The true stress value of GS Ti64 is slightly higher than that of CG Ti64.

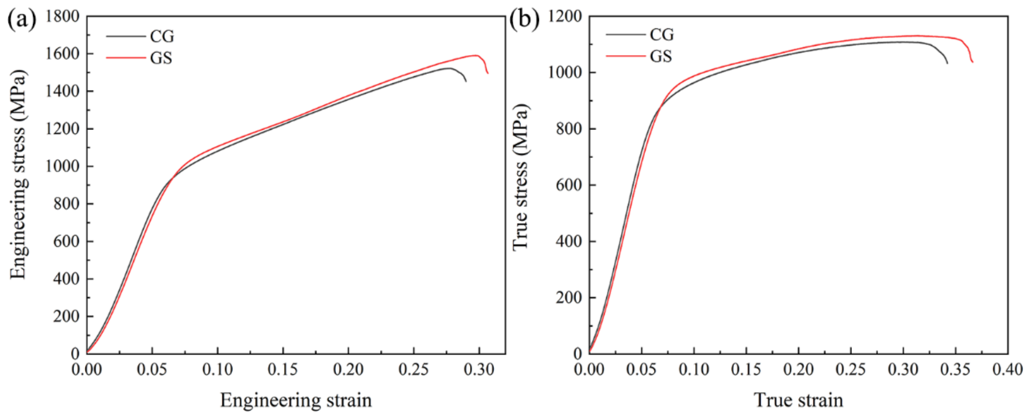

Figure 6. Representative quasi-static compression stress-strain curves of CG Ti64 and GS Ti64: (**a**) engineering stress-strain curves; (**b**) true stress-strain curves.

Figure 7 shows the true stress-strain curves of CG Ti64 and GS Ti64 at 1500 s^{-1}, 2000 s^{-1}, 2500 s^{-1} and 2700 s^{-1}. CG Ti64 and GS Ti64 show a weak strain hardening effect, the stress increases slowly with the increase of strain. When the strain rate increases to 2700 s^{-1}, CG Ti64 and GS Ti64 show ideal plastic behavior at the initial stage of plastic deformation, and obvious softening behavior occurs as the deformation continues. The sudden drop of flow stress occurred at a specific strain, indicating that local plastic instability occurs during the deformation process. The sudden drop of stress can be used as a sign of ASB formation, and further microscopic observation is needed to confirm the formation of ASB. CG Ti64 shows positive strain rate sensitivity, while GS Ti64 shows insensitivity to strain rate sensitivity. The possible reason is that the softening effect of the gradient structure layer is stronger than the work hardening effect with the increase of strain rate, resulting in no significant increase of stress.

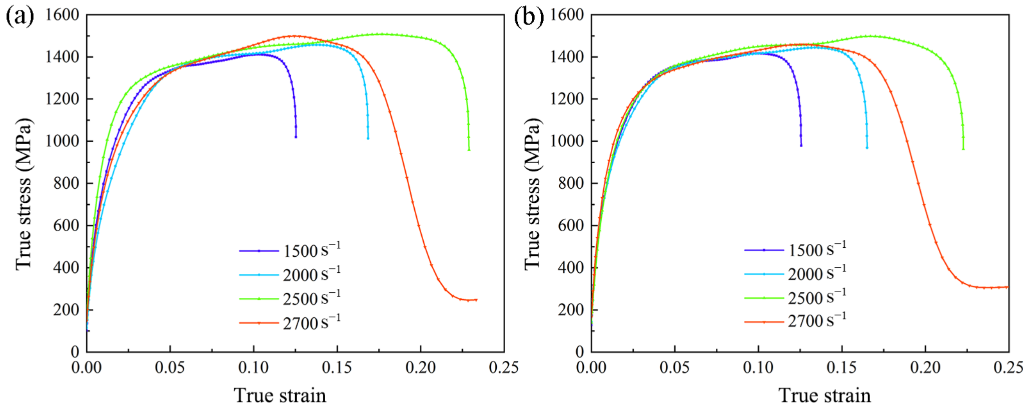

Figure 7. Representative dynamic compression true stress-strain curves: (**a**) CG Ti64 and (**b**) GS Ti64.

The average flow stress values of CG Ti64 and GS Ti64 at different strain rates are shown in Figure 8. When the strain rate is 1500 s^{-1}, the true stress of GS Ti64 is slightly higher than that of CG Ti64, and the average flow stress increases from 1365 MPa of CG Ti64 to 1386 MPa of GS Ti64. The average flow stresses are almost equal when the strain rates are 2000 s^{-1} and 2500 s^{-1}. It's worth noting that the average flow stress of GS Ti64 is less than that of CG Ti64 under 2700 s^{-1}, which is due to the stronger dynamic softening effect of GS Ti64 than CG Ti64.

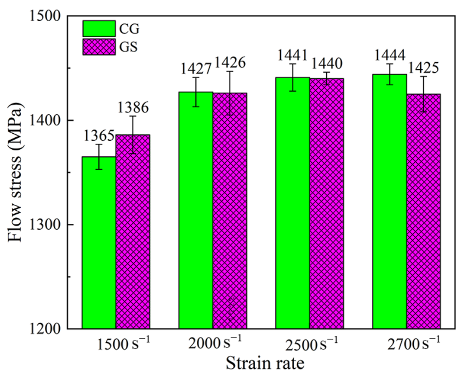

Figure 8. Flow stress of CG Ti64 and GS Ti64 under different strain rate compression.

Microscopic metallographs of longitudinally sectioned samples of CG Ti64 and GS Ti64 after compression at different strain rates are shown in Figures 9 and 10, respectively. CG Ti64 and GS Ti64 maintain uniform compression deformation at 1500 s^{-1}, 2000 s^{-1} and 2500 s^{-1}, and no ASB is generated. When the strain rate increased to 2700 s^{-1}, some saw-tooth chips formed at the two end faces of CG Ti64, coarse crack formed on the left side of the specimen, and multiple ASBs were formed on the right side (Figure 9d). By contrast, one side of the GS Ti64 sample produced some saw-tooth chips and formed a crack. The width of the crack gradually widened from the surface to the internal, the crack tip was passivated in the coarse grain region. Only one ASB was produced on the other side (Figure 10d). In addition, CG Ti64 formed a large crack and the cracks were fully opened (Figure 9d), while GS Ti64 formed small cracks (Figure 10d) in the middle of the sample, indicating that GS Ti64 has better resistance to failure. The above deformation features indicate that coordinated deformation occurs between the gradient structure and the coarse grains of the core, which prevents the premature failure of the sample.

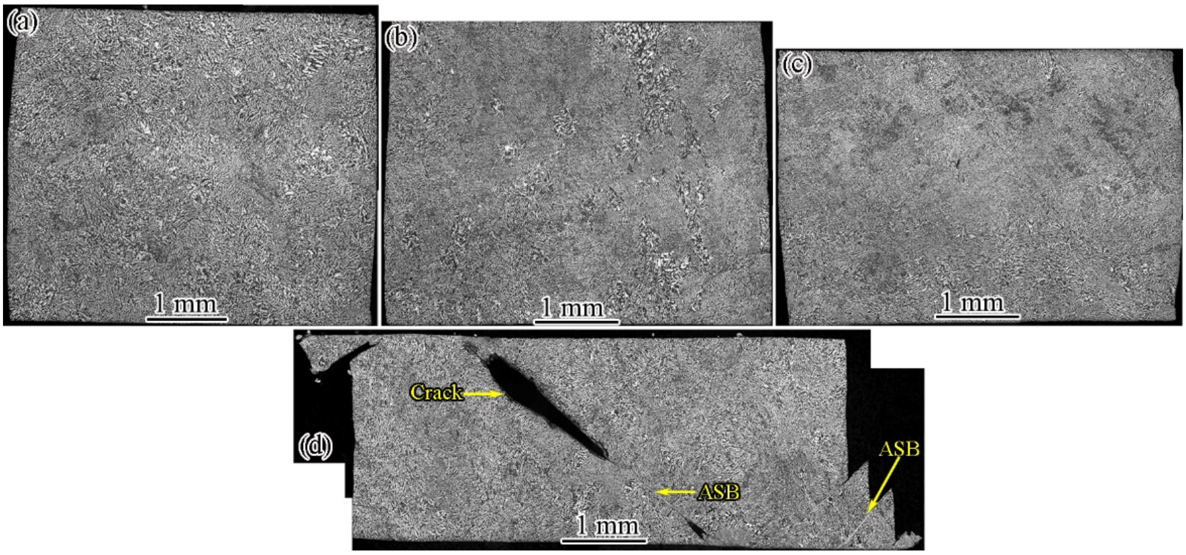

Figure 9. Micrographs of the half-sectioned area of the dynamically-compressed CG Ti64 at sequential strain rates of (**a**) 1500 s^{-1}; (**b**) 2000 s^{-1}; (**c**) 2500 s^{-1}; (**d**) 2700 s^{-1}.

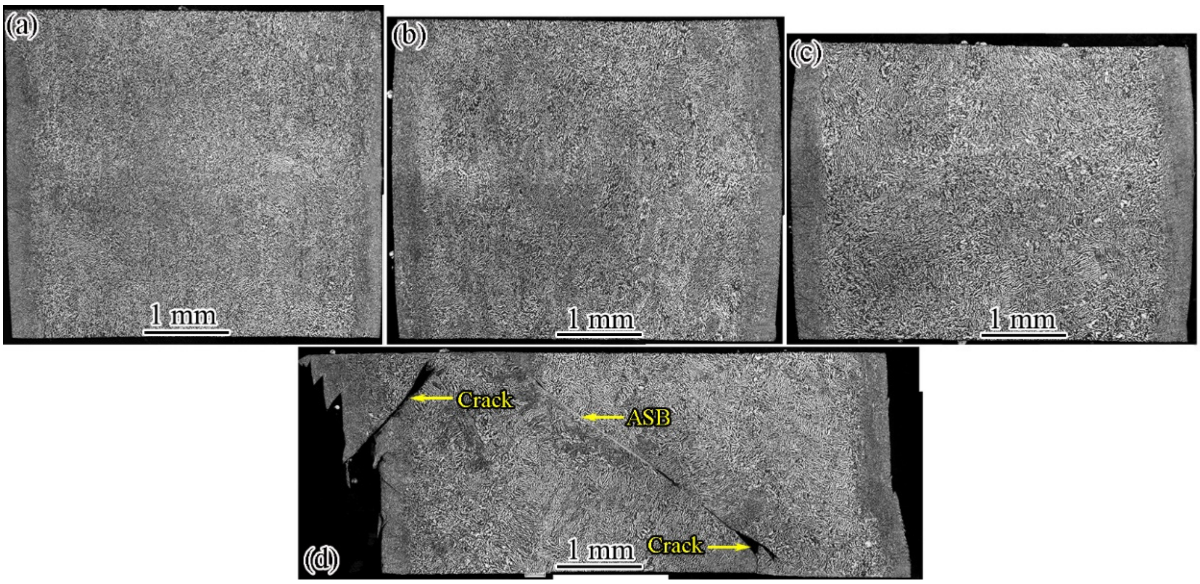

Figure 10. Micrographs of the half-sectioned area of the dynamically-compressed GS Ti64 at sequential strain rates of (**a**) 1500 s^{-1}; (**b**) 2000 s^{-1}; (**c**) 2500 s^{-1}; (**d**) 2700 s^{-1}.

The microstructures of the upper and middle regions near the sample surface of the cross-section of CG Ti64 and GS Ti64 samples after compression deformation at 1500 s^{-1}, 2000 s^{-1} and 2500 s^{-1} are shown in Figure 11. It was found that the side expansion of CG Ti64 is obvious (Figure 11a–f), while the side of GS Ti64 is relatively straight (Figure 11g–l), indicating that the gradient structure hinders the lateral expansion of the sample, resulting in more uniform compression deformation. It was also found that cracks appear on the surface of 2500 s^{-1} compression deformation (Figure 11l), indicating the difficult deformation characteristics of the surface gradient structure, which is consistent with the high hardness of the surface.

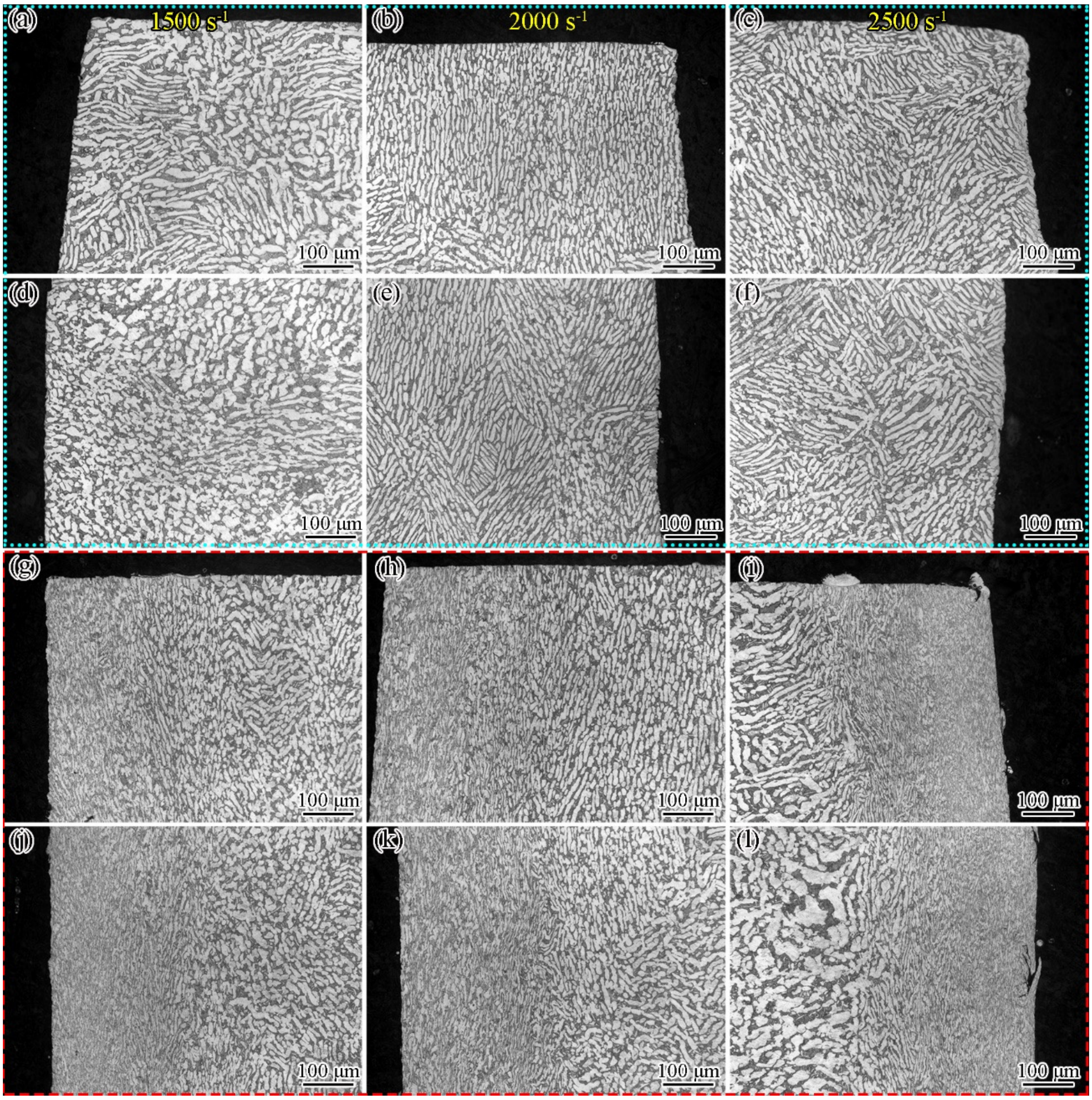

Figure 11. Microstructures near the sides of the middle part and the upper part after dynamic compression of the Ti-6Al-4V alloy: (**a**–**f**) CG Ti64; (**g**–**l**) GS Ti64.

In order to analyze the deformation mechanism within the gradient structured layer, the microstructure (at a depth of about 20 μm from the surface) before and after compression deformation is characterized by TEM, as shown in Figure 12. It can be seen that the α phase of the original large block structure produced a large number of dislocation cells and locally deformed bands (Figure 12a), and formed fine equiaxed nanocrystals in some severely deformed regions after dynamic compression (Figure 12b). The lamellar structure in the β_t transformed into equiaxed crystals (Figure 12d), and a large number of dislocations were formed inside some grains (Figure 12c,d). The results show that dynamic recrystallization of GS Ti64 gradient structure layer occurs during dynamic compression deformation. The main driving forces are the increased interface energy, distortion energy after microstructure refinement and the adiabatic temperature rise during deformation.

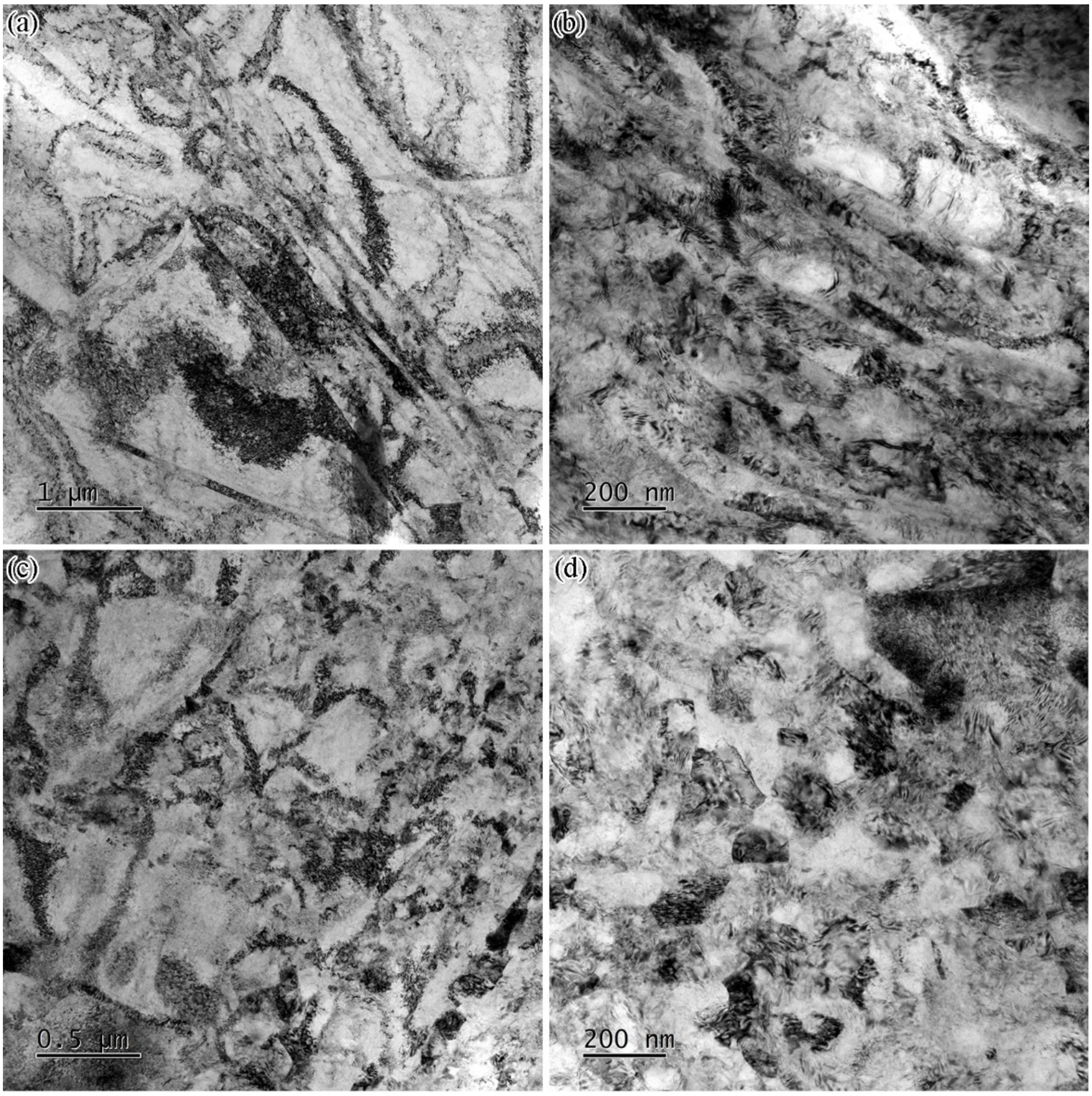

Figure 12. TEM images of GS Ti64 samples at a depth of about 20 μm from the surface before and after compression: (**a**,**b**) before compression; (**c**,**d**) after compression.

To analyze the failure mechanism of GS Ti64, the metallographs of longitudinally sectioned specimen after compression at 2700 s^{-1} are shown in Figure 13. Multiple ASBs were formed at the two end faces of the sample, and cracks along the ASB were formed (Figure 13a). The coarse crack bifurcates in the propagation process to form multiple small cracks, and a small ASB was formed at the tip of the small crack after bifurcation (Figure 13b,d). In addition, the microstructure at the crack bifurcation site was seriously twisted, which indicates that the microstructure hinders crack propagation. A relatively thick main ASB (about 25 μm wide) was formed in the middle of the sample, in which cracks extended along the shear band (Figure 13c). If the strain rate continues to increase, the cracks will penetrate the whole ASB and cause the fracture of the sample.

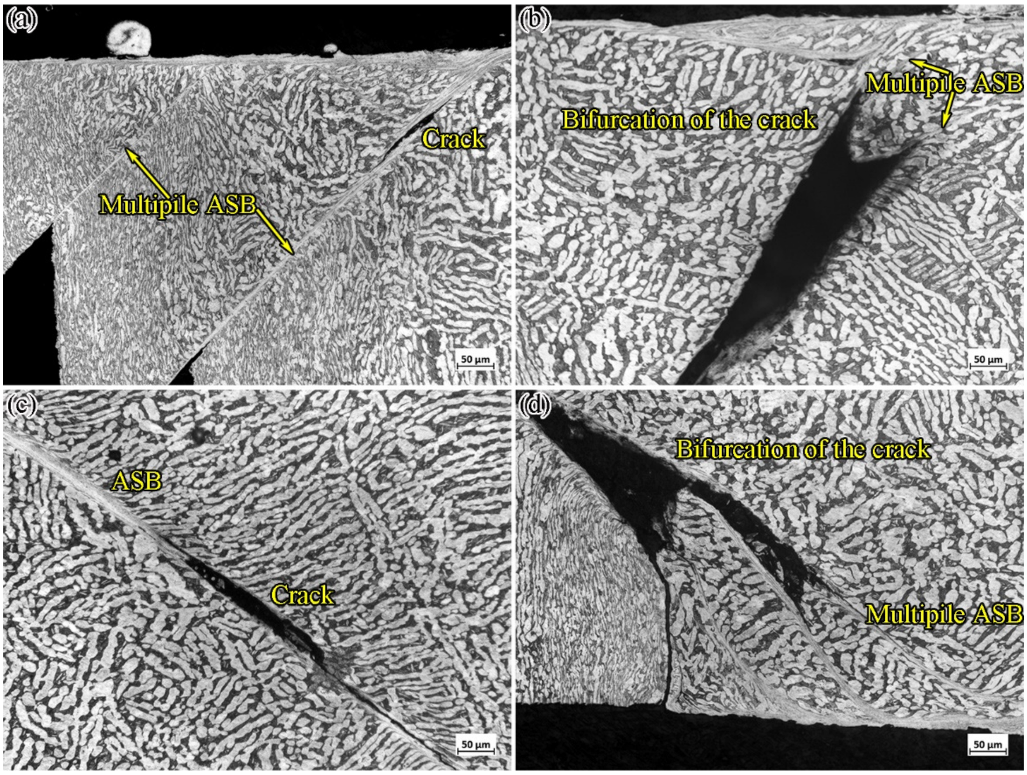

Figure 13. ASB morphology of GS Ti64 after 2700 s^{-1} dynamic compression deformation: (**a**) formation of multiple ASBs; (**b**) bifurcation of crack; (**c**) crack propagation along the ASB; (**d**) multiple ASBs are formed at the crack tip.

Interestingly, the work hardening rate of GS Ti64 is higher than that of CG Ti64 under dynamic compression (Figure 14), which differs from the general observation that the strain hardening behavior disappears and that sometimes even the strain softening behavior occurs in ultra-fine grain or nanocrystal grain under dynamic compression [9,24–26]. The strain-softening behavior of UFG and NG metals under dynamic compression is mainly due to thermal softening and the formation of ASB [27,28]. However, the strain localization trend and ASB for the surface layer of the GS Ti64 are suppressed by the CG center and the mechanical constraint is generated between different layers in the GS Ti64.

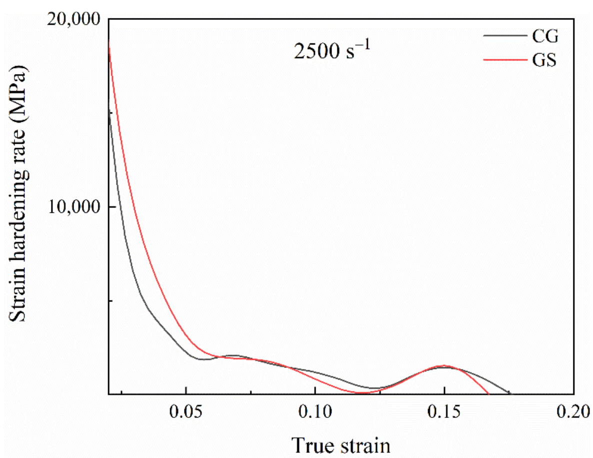

Figure 14. Strain hardening rate curves of CG Ti64 and GS Ti64 under 2500 s^{-1}.

Thus, based on these observations mentioned above, the good dynamic mechanical properties of GS Ti64 are attributed to the following aspects: (1) the CG center provides the important part of the strain hardening ability for the GS Ti64; (2) due to the large strength difference between hard surface and soft core, the resulting back stress leads to significant accumulation of geometrically necessary dislocation [29–32], which effectively increases the upper limit of allowable dislocation density in CG core and leads to a higher work hardening rate; (3) the inhibition of dynamic dislocation recovery at high strain rates and plastic deformation of grains in gradient structure also contribute to strain hardening under dynamic conditions.

4. Conclusions

In this study, gradient-structured Ti-6Al-4V was fabricated using USRP and the gradient structure was characterized by OM, EBSD, TEM and microhardness measurements. The quasi-static, dynamic compressive properties and deformation mechanisms of coarse-grained Ti-6Al-4V and gradient-structured Ti-6Al-4V were investigated in detail. The main conclusions are:

(1) A gradient layer of 293 μm thickness is formed on the surface of the Ti-6Al-4V alloy after USRP treatment. The gradient layer exhibits multi-gradient features along the depth, including the grain size gradient, strain gradient and hardness gradient.
(2) The quasi-static compressive strength of GS Ti64 (1590 MPa ± 22 MPa) is higher than that of CG Ti64 (1520 MPa ± 15 MPa), and the strain at which failure occurs is greater than that of CG Ti64, the gradient structure improves the compression properties of Ti-6Al-4V. Both CG Ti64 and GS Ti64 exhibit weak strain hardening effects and strain rate insensitivity during dynamic compression. Sudden stress drop phenomenon occurs under 2700 s^{-1} and forms ASB.
(3) The block structure of α phase in the gradient structure produces a large number of dislocation cells, local deformation bands after dynamic compression, and the lamellar structure in β_t is transformed into ultrafine crystals.
(4) Some saw-tooth chips form at the two end faces of CG Ti64 under 2700 s^{-1}. By contrast, one side of the GS Ti64 sample produces some saw-tooth chips and multiple ABS, and only one ABS is formed on the other side. In addition, CG Ti64 formed large cracks and the cracks are fully opened, while GS Ti64 forms small cracks. These deformation features indicate that coordinated deformation occurs between the gradient structure and the coarse grains, which prevents the premature failure of the sample.

The gradient structure promotes uniform compression deformation and prevents premature shear failure, but does not significantly improve mechanical properties of the alloy. In future work, on the one hand, the rolling process should be optimized to improve its dynamic mechanical properties. On the other hand, the effect of gradient structure on the dynamic mechanical properties of other titanium alloys should be studied.

Author Contributions: Conceptualization, writing—original draft, L.L.; conceptualization, methodology, investigation, writing—review & editing, supervision, and funding acquisition, Y.Z.; investigation, Q.Z.; methodology, investigation, S.X.; methodology, investigation, C.W.; methodology, formal analysis, W.J.; investigation, W.Z. All authors have read and agreed to the published version of the manuscript.

Funding: This material is based upon work supported by the Major Science and Technology Projects of Shaanxi Province of China, grant number 2020ZDZX04-01-02.

Institutional Review Board Statement: Not applicable.

Informed Consent Statement: Not applicable.

Data Availability Statement: The raw and processed data generated during this study will be made available upon reasonable request.

Conflicts of Interest: The authors declare no conflict of interest.

References

1. Cappola, J.; Stinville, J.-C.; Charpagne, M.-A.; Callahan, P.G.; Echlin, M.P.; Pollock, T.M.; Pilchak, A.; Kasemer, M. On the Localization of Plastic Strain in Microtextured Regions of Ti-6Al-4V. *Acta Mater.* **2021**, *204*, 116492. [CrossRef]
2. Chong, Y.; Deng, G.; Gao, S.; Yi, J.; Shibata, A.; Tsuji, N. Yielding nature and Hall-Petch relationships in Ti-6Al-4V alloy with fully equiaxed and bimodal microstructures. *Scr. Mater.* **2019**, *172*, 77–82. [CrossRef]
3. Shahmir, H.; Langdon, T.G. Using heat treatments, high-pressure torsion and post-deformation annealing to optimize the properties of Ti-6Al-4V alloys. *Acta Mater.* **2017**, *141*, 419–426. [CrossRef]
4. Ding, R.; Guo, Z.X.; Wilson, A. Microstructural evolution of a Ti–6Al–4V alloy during thermomechanical processing. *Mater. Sci. Eng. A* **2002**, *327*, 233–245. [CrossRef]
5. Lei, L.; Zhao, Y.; Zhao, Q.; Wu, C.; Huang, S.; Jia, W.; Zeng, W. Impact toughness and deformation modes of Ti–6Al–4V alloy with different microstructures. *Mater. Sci. Eng. A* **2021**, *801*, 140411. [CrossRef]
6. Yan, N.; Li, Z.; Xu, Y.; Meyers, M.A. Shear localization in metallic materials at high strain rates. *Prog. Mater. Sci.* **2021**, *119*, 100755. [CrossRef]
7. Lee, W.-S.; Lin, C.-F. Plastic deformation and fracture behaviour of Ti–6Al–4V alloy loaded with high strain rate under various temperatures. *Mater. Sci. Eng. A* **1998**, *241*, 48–59. [CrossRef]
8. Muiruri, A.; Maringa, M.; Du Preez, W.; Masu, L. Effect of Stress-Relieving Heat Treatment on the High Strain Rate Dynamic Compressive Properties of Additively Manufactured Ti6Al4V (ELI). *Metals* **2020**, *10*, 653. [CrossRef]
9. Long, Y.; Peng, L.; Zhang, W.; Peng, H.; Zhang, J.; Huang, X. Effect of Grain Size on the Shear Banding Behavior of Ti-6Al-4V Alloy Under Quasi-Static Compression. *Metall. Mater. Trans. A* **2020**, *51*, 2064–2071. [CrossRef]
10. Wu, S.Y.; Bie, B.X.; Fan, D.; Sun, T.; Fezzaa, K.; Feng, Z.D.; Huang, J.Y.; Luo, S.N. Dynamic shear localization of a titanium alloy under high-rate tension characterized by x-ray digital image correlation. *Mater. Charact.* **2018**, *137*, 58–66. [CrossRef]
11. Hu, H.; Xu, Z.; Dou, W.; Huang, F. Effects of strain rate and stress state on mechanical properties of Ti-6Al-4V alloy. *Int. J. Impact Eng.* **2020**, *145*, 103689. [CrossRef]
12. Lee, D.-G.; Kim, Y.G.; Nam, D.-H.; Hur, S.-M.; Lee, S. Dynamic deformation behavior and ballistic performance of Ti–6Al–4V alloy containing fine α2 (Ti_3Al) precipitates. *Mater. Sci. Eng. A* **2005**, *391*, 221–234. [CrossRef]
13. Zheng, C.; Wang, F.; Cheng, X.; Liu, J.; Liu, T.; Zhu, Z.; Yang, K.; Peng, M.; Jin, D. Capturing of the propagating processes of adiabatic shear band in Ti–6Al–4V alloys under dynamic compression. *Mater. Sci. Eng. A* **2016**, *658*, 60–67. [CrossRef]
14. Zhou, T.; Wu, J.; Che, J.; Wang, Y.; Wang, X. Dynamic shear characteristics of titanium alloy Ti-6Al-4V at large strain rates by the split Hopkinson pressure bar test. *Int. J. Impact Eng.* **2017**, *109*, 167–177. [CrossRef]
15. Peirs, J.; Tirry, W.; Amin-Ahmadi, B.; Coghe, F.; Verleysen, P.; Rabet, L.; Schryvers, D.; Degrieck, J. Microstructure of adiabatic shear bands in Ti6Al4V. *Mater. Charact.* **2013**, *75*, 79–92. [CrossRef]
16. Li, X.; Lu, L.; Li, J.; Zhang, X.; Gao, H. Mechanical properties and deformation mechanisms of gradient nanostructured metals and alloys. *Nat. Rev. Mater.* **2020**, *5*, 706–723. [CrossRef]
17. Fang, T.H.; Li, W.L.; Tao, N.R.; Lu, K. Revealing extraordinary intrinsic tensile plasticity in gradient nano-grained copper. *Science* **2011**, *331*, 1587–1590. [CrossRef]
18. Wu, X.; Jiang, P.; Chen, L.; Yuan, F.; Zhu, Y.T. Extraordinary strain hardening by gradient structure. *Proc. Natl. Acad. Sci. USA* **2014**, *111*, 7197–7201. [CrossRef]
19. Pan, Q.; Zhang, L.; Feng, R.; Lu, Q.; An, K.; Andrew, C.C.; Jonathan, D.P.; Peter, K.L.; Lu, L. Gradient-cell–structured high-entropy alloy with exceptional strength and ductility. *Science* **2021**, *374*, 984–989. [CrossRef]
20. Yuan, F.; Chen, P.; Feng, Y.; Jiang, P.; Wu, X. Strain hardening behaviors and strain rate sensitivity of gradient-grained Fe under compression over a wide range of strain rates. *Mech. Mater.* **2016**, *95*, 71–82. [CrossRef]
21. Xing, J.; Yuan, F.; Wu, X. Enhanced quasi-static and dynamic shear properties by heterogeneous gradient and lamella structures in 301 stainless steels. *Mater. Sci. Eng. A* **2017**, *680*, 305–316. [CrossRef]
22. Bian, X.; Yuan, F.; Zhu, Y.; Wu, X. Gradient structure produces superior dynamic shear properties. *Mater. Res. Lett.* **2017**, *5*, 501–507. [CrossRef]
23. Lei, L.; Zhao, Q.; Zhao, Y.; Wu, C.; Huang, S.; Jia, W.; Zeng, W. Gradient nanostructure, phase transformation, amorphization and enhanced strength-plasticity synergy of pure titanium manufactured by ultrasonic surface rolling. *J. Mater. Process. Technol.* **2022**, *299*, 117322. [CrossRef]
24. Li, Z.; Wang, B.; Zhao, S.; Valiev, R.Z.; Vecchio, K.S.; Meyers, M.A. Dynamic deformation and failure of ultrafine-grained titanium. *Acta Mater.* **2017**, *125*, 210–218. [CrossRef]
25. Long, Y.; Zhang, W.; Peng, L.; Peng, H.; Li, X.; Huang, X. Mechanical Behaviors of Ultrafine-Grained Ti-6Al-4V Alloy During Compression at Various Strain Rates. *Metall. Mater. Trans. A* **2020**, *51*, 4765–4776. [CrossRef]
26. Wei, Q.; Jiao, T.; Ramesh, K.T.; Ma, E.; Kecskes, L.J.; Magness, L.; Dowding, R.; Kazykhanov, V.U.; Valiev, R.Z. Mechanical behavior and dynamic failure of high-strength ultrafine grained tungsten under uniaxial compression. *Acta Mater.* **2006**, *54*, 77–87. [CrossRef]
27. Wu, H.; Fan, G. An overview of tailoring strain delocalization for strength-ductility synergy. *Prog. Mater. Sci.* **2020**, *113*, 100675. [CrossRef]
28. Mishra, A.; Martin, M.; Thadhani, N.N.; Kad, B.K.; Kenik, E.A.; Meyers, M.A. High-strain-rate response of ultra-fine-grained copper. *Acta Mater.* **2008**, *56*, 2770–2783. [CrossRef]

29. Hasan, M.N.; Liu, Y.F.; An, X.H.; Gu, J.; Song, M.; Cao, Y.; Li, Y.S.; Zhu, Y.T.; Liao, X.Z. Simultaneously enhancing strength and ductility of a high-entropy alloy via gradient hierarchical microstructures. *Int. J. Plast.* **2019**, *123*, 178–195. [CrossRef]
30. Lu, K. Making strong nanomaterials ductile with gradients. *Science* **2014**, *345*, 1455–1456. [CrossRef]
31. Wu, X.; Zhu, Y. Heterogeneous materials: A new class of materials with unprecedented mechanical properties. *Mater. Res. Lett.* **2017**, *5*, 527–532. [CrossRef]
32. Listyawan, T.A.; Lee, H.; Park, N.; Lee, U. Microstructure and mechanical properties of CoCrFeMnNi high entropy alloy with ultrasonic nanocrystal surface modification process. *J. Mater. Sci. Technol.* **2020**, *57*, 123–130. [CrossRef]